Dielectric Harmonic Nanoparticles: Optical Properties, Synthesis, and Applications

Yannick Mugnier, Luigi Bonacina

To cite this version:

Yannick Mugnier, Luigi Bonacina. Dielectric Harmonic Nanoparticles: Optical Properties, Synthesis, and Applications. '21st CENTURY NANOSCIENCE – A HANDBOOK', Volume 4: Low-Dimensional Materials and Morphologies, 2020. ⟨hal-02493763⟩

HAL Id: hal-02493763

https://hal.science/hal-02493763v1

Submitted on 16 Dec 2020

‘21st CENTURY NANOSCIENCE – A HANDBOOK’, Volume 4: Low-Dimensional Materials and Morphologies (Volume Four, Chapter 10)

TITLE: *Dielectric Harmonic Nanoparticles: Optical Properties, Synthesis, and Applications*

AUTHORS: Yannick Mugnier[1], Luigi Bonacina[2]

[1.] Univ. Savoie Mont Blanc, SYMME, F-74000 Annecy, France

[2] GAP-Biophotonics, University of Geneva, Geneva, Switzerland

Introduction

In the last decades, the quest for monitoring and controlling processes at the cellular and intra-cellular level has stimulated a plethora of nanophotonics approaches. To date, the most successful and widespread ones are those based on quantum dots and upconversion nanoparticles for imaging, because of their bright luminescence emission, and those using metal particles for sensing, thanks to the sensitivity of surface plasmon scattering to local environment.(Smith & Gambhir, 2017) Recently, both Rayleigh and Mie scattering from all-dielectric nanostructures have stimulated a lot of interest, primarily because of the reduced ohmic losses of these systems, their tailorable optical properties, and the compatibility of many of these materials with manufacturing techniques.(Baranov et al., 2017; Kuznetsov, Miroshnichenko, Brongersma, Kivshar, & Luk'yanchuk, 2016) Along with nanotechnology, the photonics industry has steadily evolved offering new enabling tools, including compact and cost-effective ultrashort pulse sources in a wide range of frequencies, from visible to mid-infrared. The availability of these new instruments has greatly facilitated the investigation of the nonlinear response of nanomaterials. In particular with respect to optical damage, which is often an issue under continuous excitation and with nanosecond pulses, the use of low-energy high-peak power femtosecond pulses has opened the way to safely probe a variety of nanomaterials within their transparency range and even around their resonant frequencies. Nonlinear optical observables present various advantages, including the possibility to detect background-free parametric signals at excitation wavelengths which depose no or minimal energy on the sample under investigation. Second Harmonic Generation (SHG) is by far the most exploited among these processes, because it is the easiest to obtain and collect in terms of excitation and detection settings. Increasingly, the concurrent nonlinear emissions, which accompany SHG, are becoming accessible along with the development of new laser sources. The simultaneous collection and analysis of these signals allow developing refined detection approaches for increased sensitivity and selectivity in demanding imaging applications.

This chapter introduces and describes the use of a family of dielectric metal-oxide nanoparticles, Harmonic NanoParticles (HNPs), characterized by a noncentrosymmetric crystal structure, high nonlinear optical efficiencies, and displaying a very rich nonlinear response. We begin providing a concise reminder of some fundamental nonlinear processes in optics needed to understand HNP responses to light excitation and their quantitative assessment from colloidal ensembles. Afterwards, we outline specific properties of HNP materials along with their synthesis, and finally we describe their applications for bioimaging.

Understanding the nonlinear optical response of Harmonic Nanoparticles

This section provides a concise summary of nonlinear optical processes which are observed when exciting HNPs by a pulsed femtosecond laser. Following the reasoning and symbol convention introduced by reference textbooks,(Boyd, 2003; Gubler & Bosshard, 2002) we indicate with a tilde the quantities that are rapidly oscillating in time. We can physically understand the nonlinear response of a body invested by an external oscillating field $\tilde{E}(t)$ by modelling the position $\tilde{x}(t)$ of an electron in the medium as:

$$\ddot{\tilde{x}}(t) + 2\gamma\dot{\tilde{x}}(t) + \frac{F(\tilde{x})}{m} = \frac{e\tilde{E}(t)}{m}$$

Eq. 1

This formula describes a harmonic oscillator with a dumping term proportional to γ, and a restoring force $F(\tilde{x}) = -\mathrm{m}(\,\omega_0^2\tilde{x}(t) + a\tilde{x}^2(t) - b\tilde{x}^3(t) + \cdots)$ constituted by the sum of one harmonic term, $\omega_0^2\tilde{x}(t)$ with ω_0 the single electron resonant frequency, and several anharmonic contributions, $a\tilde{x}^2(t) - b\tilde{x}^3(t) + \cdots$ where $a, b > 0$. The term on the right side in Eq.1 corresponds to the driving by the external field, with e and m the charge and mass of an electron, respectively. The corresponding potential energy function defining the electron motion, $U(\tilde{x}) = -\int \tilde{F}(\tilde{x}).d\tilde{x} = m\left(\frac{\omega_0^2\tilde{x}^2}{2} + \frac{\mathrm{a}\tilde{x}^3}{3} - \frac{\mathrm{b}\tilde{x}^4}{4} + \cdots\right)$, contains both even and odd powers of $\tilde{x}$. At low excitation intensities, the electron undergoes motions in the proximity of its equilibrium position, $\tilde{x} = 0$, and consequently the harmonic term is sufficient for describing its oscillations. The induced dipole moment, $\tilde{p}(t) = e.\tilde{x}(t)$, linearly depends on the instantaneous electric field strength $\tilde{E}(t)$. At higher intensities, however, the nonlinear components of the restoring force (*i.e.*, $a\tilde{x}^2(t) - b\tilde{x}^3(t) + \cdots$) must be included to account for the distorted motions exerted by the external field. Note that if even orders nonlinear terms are present (*e.g.*, $a \neq 0$) the potential energy function $U(\tilde{x})$ is not symmetric about 0 $\left(U(\tilde{x}) \neq U(-\tilde{x})\right)$, whereas if only odd terms are present the function is symmetric ($U(\tilde{x}) = U(-\tilde{x})$) although not harmonic in all cases. A perturbative expansion of Eq.1 to the order *n* leads to a series of electron oscillation amplitudes $x^{(1)}, \dots, x^{(n)}$ proportional to the *n*th power of the incident electric field amplitude. In the time domain, the nonlinear interaction between a single harmonic oscillator and $\tilde{E}(t)$ can be represented as an induced dipole moment $\tilde{p}_i(t)$ whose Cartesian components $i = 1,2,3$ are written as a power series in the strength of the instantaneous applied field (here and throughout the chapter we use the Einstein summation convention):

$$\tilde{p}_i(\mathrm{t}) = \epsilon_0\left(\alpha_{ij}^{(1)}\tilde{E}_j(t) + \beta_{ijk}^{(2)}\tilde{E}_j(t)\,\tilde{E}_k(t) + \gamma_{ijkl}^{(3)}\tilde{E}_j(t)\,\tilde{E}_k\,(t)\,\tilde{E}_l(t) + \cdots\right)$$

Eq. 2

In Eq. 2, ϵ_0 is the vacuum permittivity in SI units, $\alpha_{ij}^{(1)}$ the linear polarizability, $\beta_{ijk}^{(2)}$ is the second-order polarizability or first-order hyperpolarizability, and $\gamma_{ijkl}^{(3)}$ is the third-order polarizability or second-order hyperpolarizability. For a given medium, the manifestation of these different microscopic polarizabilities is directly related to the electron motion and symmetries of the potential energy function. Because accelerated charges behave as sources of electromagnetic fields, these motions are at the origin of the frequency components generated upon the interaction with the electromagnetic field. In Fig. 1, different oscillating dipole traces $\tilde{p}_i(t)$ are plotted to illustrate the scattering of both linear and newly generated nonlinear frequencies at the two lowest nonlinear orders. In the first row, the electron oscillation amplitude is described by a sinusoidal function at the fundamental frequency ω: $\sin(\omega t)$. This situation simply results in the linear scattering of the incoming frequency. The case of an asymmetric oscillation about zero is reported in the second row, here the distorted $\tilde{p}_i(\mathrm{t})$ trace is expressed as the sum of the previous sine function plus an even harmonic term, $\cos(2\omega t)$, of smaller amplitude. The presence of this new frequency component in the material response to the field, which is associated with the small peak at 2ω in the Fourier spectrum, corresponds to the SHG process. On the other hand, the addition of an odd harmonic term, $\sin(3\omega t)$ – Third Harmonic Generation (THG), to the sine function leads to a symmetric distortion about zero as reported in the third row. Purely odd harmonics spectra are characteristic of the response of centrosymmetric media, where – as one intuitively expects - the oscillating electrons experience the same dielectric environment when moving in the positive and negative directions. In general, both even and odd harmonics are present for noncentrosymmetric crystals as displayed in the bottom row of Fig. 1.

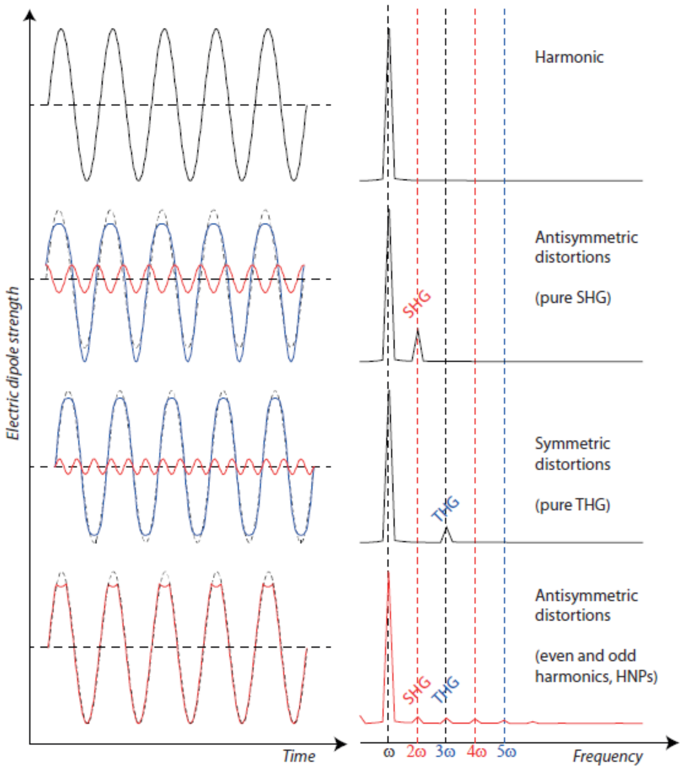

Figure 1. *First row:* the electric dipole response is linear with respect to the amplitude of the optical field. The dipole oscillations are harmonic, only the fundamental frequency ω appears in the Fourier transform plot on the right. Second row: an antisymmetric distortion appears in the oscillation pattern (blue line) because of nonlinear dependence in the field strength. This distortion can be expressed as the sum of the harmonic component (black dashed line, same as in the linear case) and a newly generated frequency at 2ω (red line). *Third row:* a purely symmetric distortion can be expressed as the sum of the harmonic component (black dashed line) and a newly generated frequency at 3ω (red line). *Fourth row:* the general case of a complex antisymmetric distortion featuring several components, similar to the case of HNPs simultaneously emitting multiple even and odd harmonics.

So far, our description assumed a single electron contribution as well as a lossless and dispersionless medium. This latter assumption is only valid when excitation and harmonic frequencies lie below the (multiple) electron resonances of the solid phase. Furthermore, additional parameters arising from the dense packing of dipoles within a lattice and from the symmetry properties of the relevant crystal class are to be considered. Instead of using electron-related variables such as $x^{(n)}$, these parameters are included in the macroscopic polarization $\tilde{P}_i(\mathrm{t}) = N.\tilde{p}_i(\mathrm{t})$ where N stands for the number density of dipoles. In analogy to Eq. 2, the instantaneous polarisation component along the i axis is written as

$$\begin{aligned}\tilde{P}_i(t) &= \epsilon_0\Big(\chi^{(1)}_{ij}\tilde{E}_j(t) + \chi^{(2)}_{ijk}\tilde{E}_j(t)\,\tilde{E}_k(t) + \chi^{(3)}_{ijkl}\tilde{E}_j(t)\,\tilde{E}_k\,(t)\,\tilde{E}_l(t) + \cdots\Big)\\ &= \tilde{P}^{(1)}_i(t) + \tilde{P}^{(2)}_i(t) + \tilde{P}^{(3)}_i(t) + \cdots\end{aligned}$$

Eq. 3

where we introduced the nonlinear susceptibilities tensors $\chi^{(n)}$ of rank $n+1$. In the linear regime, the proportionality between polarization and field is expressed through the first order susceptibility $\chi^{(1)}_{\mathrm{ij}}$, whereas second-order and third order nonlinear effects are described by the third- and the fourth-rank tensors $\chi^{(2)}_{\mathrm{ijk}}$ and $\chi^{(3)}_{\mathrm{ijkl}}$, respectively. Importantly, the number of non-zero elements for each tensor is defined by the symmetry properties of each crystal class.(Malgrange, Ricolleau, & Lefaucheux, 2012; Nye, 1985) Note also that the macroscopic electric fields used in Eq. 3 differ from the local fields defined in Eq. 2 and that appropriate local field factors accounting for the dense packing of atoms within a solid need to be introduced when replacing the microscopic polarizabilities with susceptibilities.

Equation 3 is the most comprehensive and informative expression for treating and understanding nonlinear phenomena in the perturbative regime. We point out that the presence of different conventions for defining the electric field and polarization amplitudes often complicates the comparison among experimental values from the literature. Here, the complex excitation field is described as a discrete sum of *p* monochromatic terms of frequency ω_p. The optical field strength is given by $\tilde{E}(r,t) = \frac{1}{2}\sum_p\big(E_p^{\omega_p}\ e^{-i\omega_p t} + c.c.\big)$ with $E_p^{\omega_p} = E_p^0 e^{ik_p.r}$ the spatially varying amplitude and E_p^0 the real part of the field amplitude oscillating at ω_p. Likewise, the nonlinear polarization is written as $\tilde{P}(r,t) = \frac{1}{2}\sum_p\Big(P_p^{\omega'_p}\ e^{-i\omega' t} + c.c.\Big)$ so that after expansion in Eq.3, the Fourier components of the nonlinear polarization can be derived at each nonlinear order. For instance, in the simplest case of a single input frequency component ω, the amplitude of the second-order nonlinear polarization resulting from $\widetilde{\mathrm{P}}_{\mathrm{i}}^{(2)}(\mathrm{t}) = \epsilon_0 \chi_{\mathrm{ijk}}^{(2)} \widetilde{\mathrm{E}}_{\mathrm{j}}(\mathrm{t})\, \widetilde{\mathrm{E}}_{\mathrm{k}}(\mathrm{t})$ becomes

$$P_i^{2\omega} = \frac{1}{2}\epsilon_0 \chi_{\mathrm{ijk}}^{(2)} E_j^{\omega} E_k^{\omega} = \epsilon_0 \mathrm{d}_{\mathrm{ijk}}^{(2)} E_j^{\omega} E_k^{\omega}$$

Eq. 4

This expression accounts for SHG. $\chi_{\mathrm{ijk}}^{(2)}$ is here real and frequency-independent since optical frequencies are assumed in the material transparency range and well below electron resonance frequencies (Kleinman's assumption). $\mathrm{d}_{\mathrm{ijk}}^{(2)}$ is defined as the nonlinear optical coefficient for SHG.

If we now consider a two-frequency input field (ω_1 and ω_2), the second order polarization contains the previous terms calculated for ω_1 and ω_2 independently, and new terms corresponding to their sum $\omega_1 + \omega_2$ (sum frequency generation, SFG) and difference $\omega_1 - \omega_2$ (DFG).

$$P_i^{\omega_1+\omega_2} = \epsilon_0 \chi_{\mathrm{ijk}}^{(2)} E_j^{\omega_1} E_k^{\omega_2} \quad \text{and} \quad P_i^{\omega_1-\omega_2} = \epsilon_0 \chi_{\mathrm{ijk}}^{(2)} E_j^{\omega_1} (E_k^{\omega_2})^*$$

Eq. 5

Note that the frequencies ω_1 and ω_2 are often just two distinct spectral components within the bandwidth of a femtosecond pulse. The derivation we just described to obtain the nonlinear processes at the second order can be readily repeated for the third order in the power expansion of $\tilde{P}(t)$. In this case, one obtains two families of processes, the so-called parametric ones where the total photon energy is conserved, and the non-parametric ones, where a fraction of the beam energy is transferred to the medium and which feature an imaginary component for the susceptibility $\chi^{(3)}$. To the former family belong processes like third harmonic generation ($\omega + \omega + \omega = 3\omega$, THG), all possible sum and difference combinations of three frequencies (ω_1, ω_2, and ω_3), and the intensity modulation of the refractive index (Kerr effect). The second family includes phenomena such as two-photon absorption and stimulated Raman scattering. For THG, when a unique frequency is considered, the amplitude of the third-order polarization is given by:

$$P_i^{3\omega} = \frac{1}{4}\epsilon_0 \chi_{\mathrm{ijkl}}^{(3)} E_j^{\omega} E_k^{\omega} E_l^{\omega}$$

Eq. 6

As oscillating polarization is a source of radiation, the relative strength of the *n^th^* order signal emitted by the nonlinear interaction in the medium scales as $(I_\omega)^n$ with I_ω being the intensity of the excitation field. This relationship is valid within the perturbative regime we used for all the derivations provided. Therefore, under moderate excitation conditions, the lowest order allowed by symmetry should prevail since for the anharmonic terms in the expression of the restoring force (see Eq. 1) it is expected that $\omega_0^2 \tilde{x}(t) \gg a\tilde{x}^2(t) \gg b\tilde{x}^3(t)$. This is the reason why HNPs are selected among materials possessing noncentrosymmetric crystal structure, so that they can exert second-order nonlinear response along with higher odd and even orders.

In this respect, dielectric HNPs are genuinely different from metal particles where the absence of inversion symmetry at the origin of second-order processes stems only from the particle surface and not from its inner structure. (Nappa et al., 2005) Because the crystal volume of HNP materials is by itself devoid of an inversion centre, this entails that the SHG emission intensity is essentially associated to the square of the HNP volume, V. Within the electric dipole approximation, this V^2 dependence comes from the coherent nature of signal summation over the individual nonlinear dipoles associated with each unit cell of the lattice.(Sandeau et al., 2007; Staedler et al., 2012) Similarly to their bulk counterparts, noncentrosymmetric nanocrystals are expected to exhibit large values for their second order susceptibility tensor $\chi^{(2)}$.(Joulaud et al., 2013; Le Dantec et al., 2011) On the other hand, values of the different $\chi^{(n)}$ susceptibilities are not independent. There exist some heuristic relationships for estimating the average susceptibility value at order *n* from that at *n-1*, the most famous being Miller's rule which states that $\frac{\chi^{(2)}(\omega_1+\omega_2,\omega_1,\omega_2)}{\chi^{(1)}(\omega_1+\omega_2)\chi^{(1)}(\omega_1)\chi^{(1)}(\omega_2)}$ is a constant for all noncentroysmmetric crystals if they are probed out of resonance. Similarly, some authors have observed that $|\chi^{(3)}| \propto |\chi^{(2)}|^2$for frequencies in the transparent range of noncentrosymmetric materials characterized by $|\chi^{(2)}| \geq 10^{-12}$ pm/V.(Morita & Yamashita, 1993) It is therefore a reasonable assumption that all HNP materials display both large $|\chi^{(2)}|$ and $|\chi^{(3)}|$ values simultaneously. This, in turn, means that HNPs simultaneously generate strong, volume-dependent SHG and THG signals. In quantitative terms, the SHG/THG ratio scales as $\frac{I_{3\omega}}{I_{2\omega}} \propto I_\omega$ so that high excitation intensities achievable under tight focusing conditions tend to favour the higher order, as recently confirmed by the detection of the fourth order response of individual HNPs.(Riporto et al., 2018) Moreover, one cannot fully neglect the existence of resonances in the material, which can selectively enhance the response at specific range of frequencies.

HNP materials and synthesis

Most HNP materials belong to the family of metal oxides and their crystal classes do not show inversion symmetry. Because of that, they are not only SHG-active but they also exhibit a series of functional characteristics (piezoelectricity, ferroelectricity, electro-optical properties …) exploited in many sensor and transducer applications that typically require bulk crystals or ceramics. High-temperature and long-time processing methods have been developed for the preparation of these multifunctional materials. Unfortunately, crystal-growth techniques and solid-state chemistry approaches leading to controlled size and shape are very limited at the nanoscale. Ideally, for HNPs, monodisperse and monocrystalline nanoparticles of well-defined morphology and chemical composition corresponding to mixed-metal oxide phases are required such as those of the perovskite group (*e.g.*, Barium Titanate: $BaTiO_3$) and the solid solutions belonging to the titanate, zirconate and PZT families. Lead-free niobate and tantalate materials derived from $KNbO_3$ and $KTaO_3$ are also potential candidates (Lombardi, Pearsall, Li, & O'Brien, 2016; Modeshia & Walton, 2010) and among other transition-metal perovskites, Bismuth Ferrite ($BiFeO_3$) possesses remarkable SH and TH properties.(Clarke et al., 2018; Schmidt et al., 2016) Several non-perovskite structure materials like $LiNBO_3$, ZnO, and $Fe(IO_3)_3$ have also been investigated.

For all these oxides and mixed-metal oxides, wet chemical routes are preferred since a homogenous, stoichiometric metal precursor containing two or more cations is more likely to be achieved from the liquid state. These approaches include chemical reactions in nanostructured-media and sol-gel chemistry employing a large panel of organic additives and/or relying on the systematic variation of several parameters such as the composition of the reaction medium and its temperature.(Danks, Hall, & Schnepp, 2016; Modeshia & Walton, 2010) Mild conditions associated with the hydro- and solvo-thermal processes combined with conventional furnaces or microwave heating are also increasingly applied for adjusting the nucleation and growth kinetics, and promoting crystallization without the need of a high-temperature calcination step.(Danks et al., 2016) The production of HNPs of tailored size, shape, and morphology ultimately relies on the elucidation of the reaction(Niederberger & Garnweitner, 2006) and growth mechanisms, which may comprise of a combination of several phenomena including aggregation-induced crystallization, oriented-attachment, dissolution-precipitation and Ostwald ripening.

In practice, such a detailed understanding of the growth mechanisms requires extensive time-resolved measurements and there is no general rule for the above-cited HNP materials in spite of the increasing available literature, which also includes several reviews.(Rachid Ladj et al., 2013; Modeshia & Walton, 2010; Polking, Alivisatos, & Ramesh, 2015) A given material may indeed display a very different crystallization pathway depending on the details of the solution-mediated route applied. We outline below the most common ones present in the literature with some examples relevant for HNP synthesis.

i) Regarding coprecipitation reactions and the use of nanostructured reaction media like Water-in-Oil microemulsions, Second Harmonic Scattering (see next section) has proven to be very useful to probe in real-time the crystallization dynamics of $Fe(IO_3)_3$. An aggregation-induced crystallization mechanism has been proposed to account for the particle growth and appearance of different hierarchically organized hybrid superstructures.(R Ladj et al., 2012; Mugnier et al., 2011) For $BiFeO_3$, solubility issues might explain the formation of stoichiometric amorphous hydroxide precursors after the room-temperature coprecipitation of Fe^{3+} and Bi^{3+} ions in homogeneous solutions but the subsequent high-temperature crystallization step only results in poorly shape-defined NPs without addition of organic additives.(Tytus et al., 2018) Noteworthy, in the case of lithium niobate and lithium tantalate ($LiNbO_3$, $LiTaO_3$), if the prerequisite of a homogeneous dispersion of the metal precursors at the atomic scale is not fulfilled, for instance when the

Li:Nb (resp. Li:Ta) ratio is different from 1:1 with the Nb-rich hexaniobate (resp. Ta-rich hexatantalate) Lindqvist ions, the aqueous synthesis of phase-pure $LiNbO_3$ (resp. $LiTaO_3$) is prevented.(Nyman, Anderson, & Provencio, 2009)

ii) The traditional sol-gel chemistry route leading to monometallic oxide materials(Livage & Sanchez, 1992) from alkoxide precursors has been successfully extended to bimetallic oxides like $LiNbO_3$ films.(Ono & Hirano, 1997) For this approach, the availability and cost of the metal elements that can be used as alkoxide precursors and their high degree of reactivity with water are first to be considered. The initial hydrolysis and condensation reactions that are supposed to lead to the desired stoichiometric mixed-metal ABO_3 phase actually depend on several experimental parameters including the element electronegativity, the amount of water and its pH, the solvent polarity, and the use of chelating agents. The detailed growth mechanisms are not always fully understood but a series of very convincing results have recently been reported for $LiNbO_3$,(Mohanty et al., 2012) derivatives of $KNbO_3$, (Lombardi et al., 2016) and $BaTiO_3$.(S. Liu et al., 2015) Similarly, oleic acid-assisted hydrothermal treatments of precipitates resulting from the fast reaction between aqueous metal nitrates and butoxides result in well-defined cubic and spherical $BaTiO_3$ nanocrystals of varying sizes according to the nature of the solvent and co-solvent.(Caruntu, Rostamzadeh, Costanzo, Parizi, & Caruntu, 2015) In the case of $LiNbO_3$, when benzyl alcohol is first applied to reduce the niobium ethoxide reactivity, the subsequent addition of triethylamine as a surfactant allows mediating the growth under solvothermal conditions after passivation of the nanocrystal surface. Transformation of the initial lithium and niobium hydroxide precursors to partially crystallized aggregates, and finally to monocristalline nanoparticles of different size, likely results in a combination of the aggregation-induced crystallization, oriented-attachment, and Ostwald ripening processes.(Ali & Gates, 2018)

iii) Several chelating agents are also effective for stabilizing metal complexes from water-soluble metal salts to circumvent some of the inherent limitations of the alkoxide-based sol–gel route. In the case of $BiFeO_3$, this small molecule approach(Danks et al., 2016) has been initiated by Ghosh (Ghosh, Dasgupta, Sen, & Sekhar Maiti, 2005) and Selbach (Selbach, Einarsrud, Tybell, & Grande, 2007) with citric acid and a series of carboxylic acids with or without deliberate addition of extra hydroxyl groups. Both phase-pure and mixed-phase compounds can be obtained with an average crystallite size that increases with the annealing temperature as expected for an Ostwald ripening process for relatively aggregated products. This solvent evaporation route with metal complexes has then been further refined with mucic acid and NaCl in excess to promote the formation of phase-pure, monocrystalline and SHG-efficient $BiFeO_3$ HNPs.(Clarke et al., 2018) Note also that ethylenediaminetetraacetic acid (EDTA) is another example of commonly used chelating agent that has a key role in the solvothermal synthesis of several perovskite-type nanomaterials.(Modeshia & Walton, 2010)

iv) Finally, the controlled formation of mixed-metal oxides from homogeneously dispersed metals in a polymeric precursor can be achieved from the Pechini method. Typically, citric acid is used as previously explained as a chelating agent to form metal citrate complexes, but a polymerizer like ethylene glycol is then added to initiate polyesterifcation upon heating. The as-obtained covalent organic network is expected to be more stable during annealing thus giving more opportunities to control the crystallization and growth mechanisms. Note that many other available carboxylic acids and polyols can be used in place of citric acid and ethylene glycol, respectively. For $LiNbO_3$, calcination in air of the gel precursor requires high temperature (>450°C) and the resulting dried nanopowder then consists of aggregated nanocrystals.(Yerlikaya, Ullah, Kamali, & Kumar, 2016) The lowest crystallization temperature achievable for $BiFeO_3$ has been found to strongly depend on the structure of the chelating agent and when glycerol is added to promote polyesterification with the mucic acid, mixed phase products and the absence of any size and shape control can be noticed after the gel combustion.(Clarke et al., 2018; Selbach et al., 2007) Very likely, ill-defined local thermodynamic conditions and a non-uniform temperature during the combustion step account for the presence of impurities as already observed when the complexing agent is replaced by a fuel.(Schwung et al., 2014)

Quantitative assessments of $\chi^{(2)}$ and $\chi^{(3)}$ values from colloidal HNP suspensions

Once HNP samples are obtained, the quantitative assessments of the orientation-averaged second- and third-order susceptibilities can be obtained by SH and TH Scattering (SHS and THS) measurements provided that colloidal HNP suspensions of known particle size and mass concentration are available. Noteworthy, SH and TH efficiencies determined by this approach have been found in very good agreement with the literature values on bulk crystals, at least for nanocrystal size larger than 10 nm. We also want to emphasize that, contrary to this ‘ensemble measurement’ approach, imaging of individual HNPs based on SHG and THG microscopy techniques is less prone to provide reliable results on nonlinear efficiencies. In this case, in fact, a proper modelling of the focusing and collection properties at each nonlinear order needs to be introduced, especially when dealing with diffraction-limited objects. Moreover, when imaging individual nanoparticles because of the tensorial nature of the different harmonic processes, the polarization-resolved traces one obtains should be fitted with mathematical expressions whose complexity rapidly increases with the non-linear order and with the number of independent coefficients of the relevant crystal class.(Bonacina et al., 2007; Le Floc'h, Brasselet, Roch, & Zyss, 2003; Schmidt et al., 2016)

Historically, harmonic light scattering from molecules in solutions (successively referred to Hyper-Rayleigh Scattering, HRS), firstly observed in 1965, (Terhune, Maker, & Savage, 1965) paved the way to SHS and THS experiments on colloidal suspensions of NPs. HRS was applied during the nineties to determine the second-order polarizability of nonpolar molecules.(Clays & Persoons, 1991; Hendrickx, Clays, & Persoons, 1998) The HRS intensity $I_{2\omega}$ stems from the incoherent SH signal contributions scattered by the individual sources at concentration N_m with a squared dependence on the incident intensity I_ω: $I_{2\omega} = G_{2\omega}.\lambda_{2\omega}^{-4}.N_m.F_m^2.\langle\left(\beta^{(2)}\right)^2\rangle.I_\omega^2$. The local field factors included in $F_m = f_\omega^2.f_{2\omega}$, account for the microscopic optical field experienced by each molecule, $G_{2\omega}$ comprises the experimental collection efficiency and other constant factors, while $\langle\left(\beta^{(2)}\right)^2\rangle$ is the squared hyperpolarizability isotropically averaged over all orientations.(Cyvin, Rauch, & Decius, 1965) Keeping the original HRS experimental configuration, which implies the collection of $I_{2\omega}$ perpendicularly to the excitation beam, HRS was successively extended to larger objects (Deniset-Besseau et al., 2009; Jacobsohn & Banin, 2000; Russier-Antoine, Benichou, Bachelier, Jonin, & Brevet, 2007) and nanocrystal suspensions.(Le Dantec et al., 2011; Rodriguez, de Araújo, Brito-Silva, Ivanenko, & Lipovskii, 2009) In the latter case, the introduction of an effective hyperpolarizability term proportional to the nanoparticle volume *V* conveniently upgrades the original HRS formalism (developed for molecular dipoles oscillating at 2ω) to the solid-state phase, filling the gap between microscopic and macroscopic entities. When HNPs are large enough to neglect surface contribution (roughly > 20 nm),(Kim et al., 2013; Knabe, Buse, Assenmacher, & Mader, 2012) the scattered SH signal can be expressed as above, *viz.* $I_{2\omega} = G_{2\omega}.\lambda_{2\omega}^{-4}.N_{NP}.T_{NP}^{2}.\langle\left(\beta_{NP}^{(2)}\right)^{2}\rangle.I_{\omega}^{2}$ where $\langle\beta_{NP}^{(2)}\rangle$ is the volume-dependent hyperpolarizability given by $\langle\beta_{NP}^{(2)}\rangle = \sqrt{\langle\left(\beta_{NP}^{(2)}\right)^{2}\rangle} = \langle d_{NP}^{(2)}\rangle.V$. Because of its size dependence, $\langle\beta_{NP}^{(2)}\rangle$ is not an intrinsic material property as it represents - in the Rayleigh regime(Roke & Gonella, 2012) - the coherent contribution of the induced dipole moments within each unit cell of the nanoparticle lattice.(Joulaud et al., 2013; Le Dantec et al., 2011) In line with the previous expression, $\langle d_{NP}^{(2)}\rangle$ is the orientation-averaged SH coefficient linked to the second order susceptibility by $\langle\chi_{NP}^{(2)}\rangle = 2\langle d_{NP}^{(2)}\rangle$. The SHS intensity $I_{2\omega}$ that linearly depends on the number density N_{NP} of HNPs can now be written as $I_{2\omega} = \frac{1}{4}.G_{2\omega}.\lambda_{2\omega}^{-4}.N_{NP}.T_{NP}^{2}\langle(\chi_{NP}^{(2)})^{2}\rangle.V^{2}.I_{\omega}^{2}$, where the coherent contribution from the volume comes along with the V^{2} term and where the local (molecular) field factors included in F_m are now replaced by reduction field factors included in T_{NP} to account for the refractive index change. The macroscopic optical excitation field E_j^{ω} within the NP volume is indeed given by $E_j^{\omega} = t_{\omega}.E_{j,inc}^{\omega}$, with $E_{j,inc}^{\omega}$ the incident optical field. Assuming quasi-spherical NPs, t_{ω} can be expressed as $t_{\omega} = \frac{3n_{sol}^{2}(\omega)}{2n_{sol}^{2}(\omega)+n_{NP}^{2}(\omega)}$ where $n_{sol}(\omega)$ and $n_{NP(\omega)}$ stand for the solvent and nanoparticle average refractive index at ω, respectively. In addition, when dispersion of the refractive index is considered in the vicinity of electron resonances (*i.e.*, $n(\omega) \neq n(2\omega)$), the reduction field factor becomes $\mathrm{T}_{NP} = \mathrm{t}_{\omega}^{2}.\mathrm{t}_{2\omega}$.

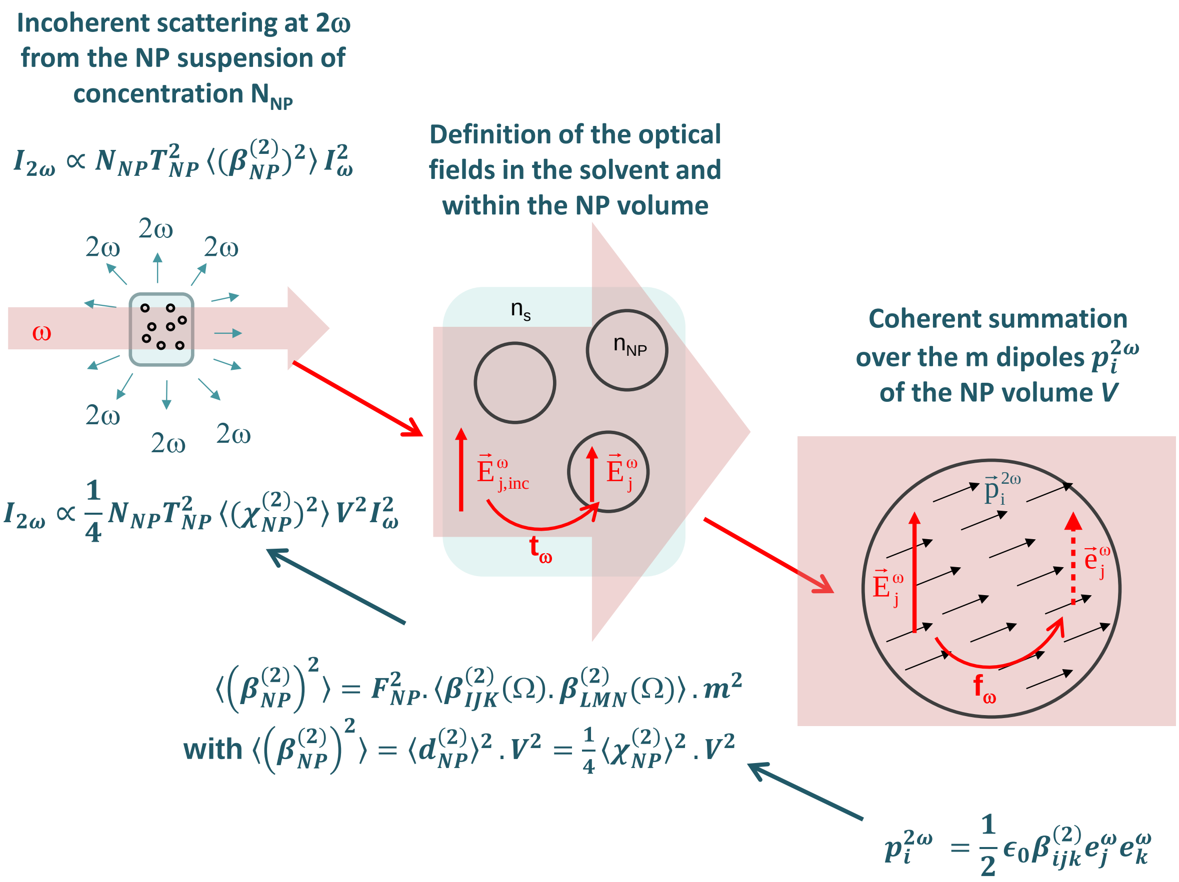

Figure 2. Principle of the SHS technique on colloidal suspensions of HNPs and definition of the different optical fields and physical entities.

Regarding THS measurements, a very similar formalism can be applied by using $I_{3\omega} = \frac{1}{16} . G_{3\omega} . \lambda_{3\omega}^{-4} . N_{NP} . T_{NP}^2 \langle(\chi_{NPs}^{(3)})^2\rangle . V^2 . I_\omega^3$ where the 1/16 pre-factor is given within the convention used by Bosshard *et al.,(Bosshard, Gubler, Kaatz, Mazerant, & Meier, 2000)* and with $T_{NP} = \mathrm{t}_\omega^3 . \mathrm{t}_{3\omega}$. The ratio between the two scattered harmonic signals $I_{2\omega}$ and $I_{3\omega}$ can be used as an approximate estimate of $\langle\chi_{NP}^{(3)}\rangle = \sqrt{\langle(\chi_{NP}^{(3)})^2\rangle}$, provided that the excitation intensity I_ω is precisely known(Multian et al., 2018; Schmidt et al., 2016) and after properly accounting for the collection and detection efficiencies at 2ω and 3ω. More generally, a quantitative assessment of the second-order susceptibility $\langle\chi_{NP}^{(2)}\rangle$ can be obtained either by the internal reference method or with the external one, thanks to the availability of different reference molecules such as para-nitroaniline (pNa) which is suitable for YAG laser excitation (1064 nm). Concerning the determination of third-order susceptibilities $\langle \chi_{NP}^{(3)} \rangle$, the straightforward internal reference approach based on very common solvents has also been recently demonstrated.(Van Steerteghem, Clays, Verbiest, & Van Cleuvenbergen, 2017)

From the experimental standpoint, it is essential to point out that exclusively orientation-averaged entities can be derived from SHS and THS measurements. In the most general case, the relations between $\langle \chi_{NP}^{(2)} \rangle$ (resp. $\langle \chi_{NP}^{(3)} \rangle$) and the independent elements of the $\chi_{\mathrm{ijk}}^{(2)}$ (resp. $\chi_{\mathrm{ijkl}}^{(3)}$) tensors depend on the scattering angle, the polarization of the excitation and harmonic signals, and the crystal symmetry. For instance, if we consider materials belonging to the orthorhombic lattice system and to the *222* crystal class, one of the simplest cases in terms of number of nonzero coefficients, any twofold rotation around one of the $i = 1,2,3$ crystalline axes not only keeps constant the macroscopic (bulk) crystal morphology but also all the physical properties after application of the symmetry operator. It results that for each nonlinear order *n*, susceptibilities tensors $\chi^{(n)}$ of rank $n+1$ must be invariant in the new basis after application of the tensor transformation. For the second-order susceptibility, this transformation operator assumes the form of $\chi_{\mathrm{ijk}}^{(\mathrm{final})} = \mathrm{a}_{ip}\mathrm{a}_{jq}\mathrm{a}_{kr}\,\chi_{\mathrm{pqr}}^{(\mathrm{initial})}$. In the case of the *222* point group, this transformation rule can be applied successively with the a_{ip} coefficients of the twofold rotation matrix A_1 (around $i = 1$) and A_3 (rotation around $i = 3$). It results for a lossless material that the initial 27 (real) independent coefficients of the $\chi_{\mathrm{pqr}}^{(\mathrm{initial})}$susceptibility tensor are reduced to only five non-vanishing tensor coefficients *xyz, xzy, yzx, yxz, zxy, zyx*. If we now use the contracted Voigt notation, the initial 18 independent elements of the 3x6 $\chi_{\mathrm{il}}^{(2)}$ matrix can be reduced to three nonzero coefficients. In addition,

$\chi_{14} = \chi_{25} = \chi_{36}$ when the excitation and SH frequencies are far from electron resonances.(Boyd, 2003)

$$A_1 = \begin{pmatrix} 1 & 0 & 0 \\ 0 & -1 & 0 \\ 0 & 0 & -1 \end{pmatrix} \text{and } A_3 = \begin{pmatrix} -1 & 0 & 0 \\ 0 & -1 & 0 \\ 0 & 0 & 1 \end{pmatrix} \text{ leads to } \chi_{\mathrm{il}}^{(2)}(class\ 222) = \begin{pmatrix} 0 & 0 & 0 & \chi_{14} & 0 & 0 \\ 0 & 0 & 0 & 0 & \chi_{25} & 0 \\ 0 & 0 & 0 & 0 & 0 & \chi_{36} \end{pmatrix}$$

Among oxide materials belonging to high symmetry point groups, the $\chi_{\mathrm{il}}^{(2)}$ matrix of sillenite compounds like BSO ($Bi_{12}SiO_{20}$, …, symmetry class 23) and the one of ZnO (symmetry class 6mm) are also given below in the non-resonant case as illustrative examples.

$$\chi_{il}^{(2)}(\mathrm{BSO}) = \begin{pmatrix} 0 & 0 & 0 & \chi_{14} & 0 & 0 \\ 0 & 0 & 0 & 0 & \chi_{14} & 0 \\ 0 & 0 & 0 & 0 & 0 & \chi_{14} \end{pmatrix} \qquad \chi_{il}^{(2)}(\mathrm{ZnO}) = \begin{pmatrix} 0 & 0 & 0 & 0 & \chi_{31} & 0 \\ 0 & 0 & 0 & \chi_{31} & 0 & 0 \\ \chi_{31} & \chi_{31} & \chi_{33} & 0 & 0 & 0 \end{pmatrix}$$

Similarly, symmetry considerations and Kleinman's assumption greatly reduce the number of nonzero components for the third-order susceptibility tensors of each crystal class. After application of the transformation formula $\chi_{\mathrm{ijkl}}^{(\mathrm{final})} = \mathrm{a}_{ip}\mathrm{a}_{jq}\mathrm{a}_{kr}\mathrm{a}_{ls}\,\chi_{\mathrm{pqrs}}^{(\mathrm{initial})}$ of a fourth-rank tensor, 3 independent coefficients (instead of 2 for $\chi_{il}^{(2)}$) can be noticed in the case of ZnO in the following 3x10 $\chi_{im}^{(3)}(\mathrm{ZnO})$ third-order susceptibility matrix expressed using the convenient contracted notation introduced by Yang *et al.*.(Yang & Xie, 1995)

$$\chi_{im}^{(3)}(\mathrm{ZnO}) = \begin{pmatrix} \chi_{11} & 0 & 0 & 0 & 0 & \chi_{16} & 0 & ⅓.\chi_{11} & 0 & 0 \\ 0 & \chi_{11} & 0 & \chi_{16} & 0 & 0 & 0 & 0 & ⅓.\chi_{11} & 0 \\ 0 & 0 & \chi_{33} & 0 & \chi_{16} & 0 & \chi_{16} & 0 & 0 & 0 \end{pmatrix}$$

For SHS and THS measurements, the orientation-averaging procedure that allows deriving $\langle\chi_{NP}^{(2)}\rangle$ and $\langle\chi_{NP}^{(3)}\rangle$ is usually considered for an incident beam with a linear polarization angle γ defined in the laboratory frame. The incident (macroscopic) optical field in the laboratory frame {X,Y,Z} can be expressed in the crystal frame {x,y,z} of a single, randomly oriented HNP by applying the rotation matrix R_{Ω}, where $\Omega(\varphi,\theta,\psi)$ represent the Euler angles. Note that the excitation field is linked through f_ω to the local (microscopic) field e_j^ω experienced by each unit cell, as illustrated in Fig. 2. The induced dipole moments oscillating at 2ω given by $p_i^{2\omega} = \frac{1}{2}\epsilon_0 \beta_{\mathrm{ijk}}^{(2)} e_j^\omega e_k^\omega$ can also be expressed as the product of the 3x6 $\beta_{\mathrm{il}}^{(2)}$ matrix and a 6-component excitation-field vector defined as $\{e_{x,}^2 e_{y,}^2, e_{z,}^2, 2e_y e_z, 2e_x e_z, 2e_x e_y\}$. The transformation of these nonlinear dipoles in the laboratory frame by the application of the operator S$_\Omega$ (*i.e.,* the transpose of R$_\Omega$) allows calculating the macroscopic optical fields $E_I^{2\omega}$ through the dipole radiation formula where the unit vector (0,1,0) is used in Fig. 3 (for a collection along the Y-axis direction).

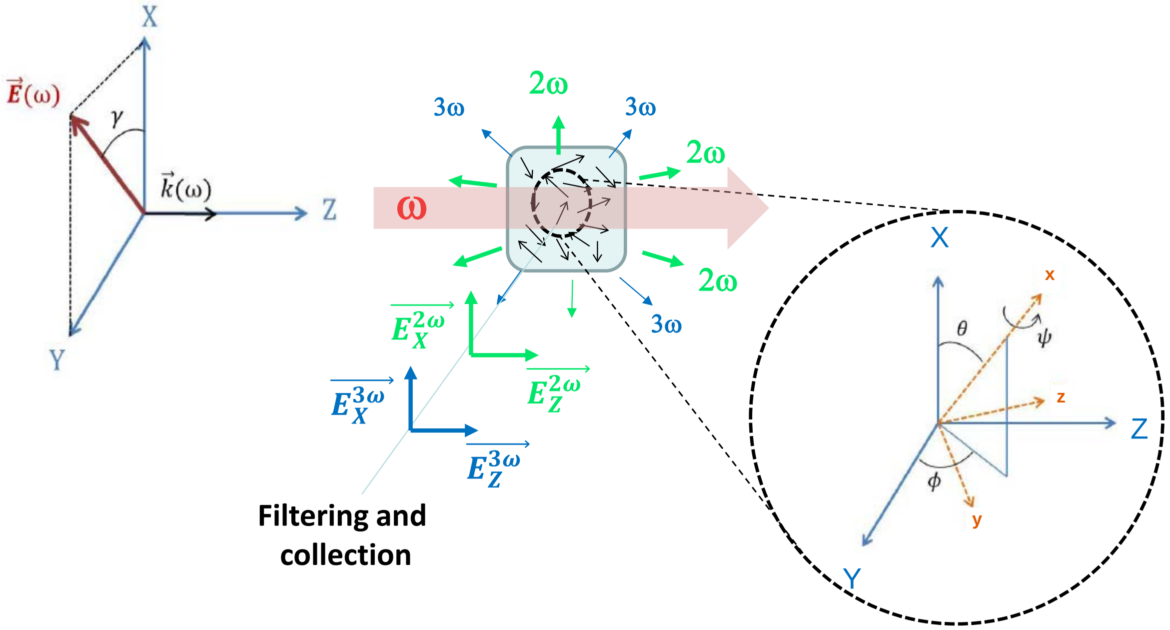

Figure 3. Experimental configuration for SHS and THS measurements with an incident linear polarization in the (X,Y) plane and a detection along the Y-axis direction. Definition of the Euler angles Ω(φ,θ,ψ) in the XYX convention leading to the orientation-averaged entities in the (macroscopic) laboratory frame {X,Y,Z}={I,J,K} from the susceptibility tensors expressed in the (microscopic) crystal frame {x,y,z}={i,j,k}

The resulting vertically-polarized SH intensity accounting for the orientation-averaging procedure is then simply calculated as $I_X^{2\omega} = \frac{1}{8\pi^2}\int_{\theta=0}^{\theta=\pi}\int_{\varphi=0}^{\varphi=2\pi}\int_{\psi=0}^{\psi=2\pi}(E_X^{2\omega})^2 . \sin\theta \, d\theta d\varphi d\psi$ whereas a similar expression applies for $I_z^{2\omega}$ with $E_Z^{2\omega}$. The above description is not only the most natural in terms of physical understanding, but also the most efficient to be numerically computed. It is of course consistent with the common alternative approach that consists in determining the macroscopic $\beta^{(2)}_{\mathrm{IJK}}$ coefficients from the corresponding $\beta^{(2)}_{\mathrm{ijk}}$ molecular components. This transformation defined by the usual tensor rotation formula $\beta^{(2)}_{\mathrm{IJK}}(\Omega) = \sum_{ijk}(S_{Ii}S_{Jj}S_{Kk})\beta^{(2)}_{ijk}$ becomes:

$$\langle\left(\beta^{(2)}\right)^2\rangle = \langle\beta^{(2)}_{\mathrm{IJK}}(\Omega).\,\beta^{(2)}_{\mathrm{LMN}}(\Omega)\rangle =$$

$$\frac{1}{8\pi^2}\int_{\theta=0}^{\theta=\pi}\int_{\varphi=0}^{\varphi=2\pi}\int_{\psi=0}^{\psi=2\pi}\sum_{ijklmn}(S_{Ii}S_{Jj}S_{Kk}S_{Ll}S_{Mm}S_{Nn})\beta^{(2)}_{ijk}\beta^{(2)}_{lmn}\,.\sin\theta\, d\theta d\varphi d\psi$$

for the squared, orientation-averaged hyperpolarizability expressed in the laboratory frame.(Cyvin et al., 1965) If we consider a colloidal suspension of nanoparticles, the coherent contribution from the *m* dipoles of the HNP volume *V* is written as $\langle\left(\beta^{(2)}_{NPs}\right)^2\rangle = F^2_{NP}.\langle\beta^{(2)}_{\mathrm{IJK}}(\Omega).\,\beta^{(2)}_{\mathrm{LMN}}(\Omega)\rangle\,.m^2 = \left\{F^2_{NP}.\langle\beta^{(2)}_{\mathrm{IJK}}(\Omega).\,\beta^{(2)}_{\mathrm{LMN}}(\Omega)\rangle\,.N^2\right\}V^2$ where the material local field factors are included in $F_{NP} = f^2_{\omega}.f_{2\omega}$ and where the number density of formula units is $N = m/V.$ The relation between the macroscopic susceptibility and the microscopic hyperpolarizability $\mathrm{d}^{(2)}_{\mathrm{IJK}} = \frac{1}{2}\chi^{(2)}_{\mathrm{IJK}} = F_{NP}.\,\beta^{(2)}_{\mathrm{IJK}}(\Omega).N$ finally results in a volume-dependent hyperpolarizability $\langle\left(\beta^{(2)}_{NPs}\right)^2\rangle = \langle d^{(2)}_{NPs}\rangle^2\,.V^2 = \frac{1}{4}\langle\chi^{(2)}_{NPs}\rangle^2\,.V^2$ as we previously discussed.

As an example, when the above formalism is applied to the ZnO case under non-resonant conditions and for a vertically polarized incident field (γ=0) with no analyser in the detection path, the square of the orientation-averaged second-order susceptibility becomes $\langle\left(\chi^{(2)}_{NP}\right)^2\rangle = \langle\left(\chi^{(2)}_{XXX}\right)^2\rangle + \langle\left(\chi^{(2)}_{ZXX}\right)^2\rangle$ with $\langle\left(\chi^{(2)}_{XXX}\right)^2\rangle = \frac{1}{7}\chi^2_{33} + \frac{24}{35}\chi^2_{31} + \frac{12}{35}\chi_{33}\chi_{31}$ and $\langle\left(\chi^{(2)}_{ZXX}\right)^2\rangle = \frac{1}{35}\chi^2_{33} + \frac{4}{21}\chi^2_{31} - \frac{4}{105}\chi_{33}\chi_{31}.$

Similarly, when $\beta_{ijk}^{(2)}\beta_{lmn}^{(2)}$ is now replaced by $\gamma_{ijkl}^{(3)}.\gamma_{mnop}^{(3)}$ in the previously defined integration and the number of rotation matrix S_{Ω} consistently increased, the square of the orientation-averaged third-order susceptibility measured with the THS configuration is expressed as $\langle\left(\chi_{NP}^{(3)}\right)^2\rangle_{THS} = \langle\left(\chi_{XXXX}^{(3)}\right)^2\rangle_{THS} + \langle\left(\chi_{ZXXX}^{(3)}\right)^2\rangle_{THS}$ with:

$$\langle\left(\chi_{XXXX}^{(3)}\right)^2\rangle_{THS} = \frac{1}{9}\chi_{33}^2 + \frac{128}{315}\chi_{11}^2 + \frac{32}{35}\chi_{16}^2 + \frac{16}{315}\chi_{33}\chi_{11} + \frac{8}{21}\chi_{33}\chi_{16} + \frac{64}{105}\chi_{11}\chi_{16}$$

$$\langle\left(\chi_{ZXXX}^{(3)}\right)^2\rangle_{THS} = \frac{1}{63}\chi_{33}^2 + \frac{8}{315}\chi_{11}^2 + \frac{1}{7}\chi_{16}^2 - \frac{8}{315}\chi_{33}\chi_{11} - \frac{2}{105}\chi_{33}\chi_{16} - \frac{8}{105}\chi_{11}\chi_{16}$$

where the independent third-order coefficients are here still expressed with the matrix notation. (Alexiewicz, Ozgo, & Kielich, 1975) (Multian et al., 2018)

Optical bio-imaging with HNPs

The choice of nanoparticles in optical bio-imaging applications over other methods (fluorescence immunostaining, fluorescent protein expression, ...) is usually motivated by one or several of the following criteria: i) need of very bright and stable emission over time; ii) access to multimodal detection; iii) application of targeting strategy (antibodies, enhanced retention, …) ; iv) use of the nanoparticles for *in situ* delivery of a molecular payload or as local triggers of a therapeutic effect. Clearly, not all these requirements are fully met by a single nanotechnological approach. The side effects of the use of nanoparticles (in terms of toxicity or other perturbation of the sample under study) should also be carefully accounted for in the choice. Based on these general considerations, the following characteristics of HNPs, discussed in the previous sections, are relevant for their selection in specific bio-imaging applications:

1. Typical size 50-200 nm, with in general a rather broad size distribution within this interval.
2. Absence of known toxic elements in their chemical composition.
3. Emission based on multiple simultaneous harmonic signals rather than luminescence.

1) The relative large dimensions of HNPs follow from the chemical synthetic protocols and is very beneficial in terms of brightness since the signal intensity scales as V^2. This volume dependence poses limitations to the detection of HNPs with diameter $\ll 50$ nm in a biological sample. Because of their typical size and not homogeneous shape distribution, HNPs are generally not the first choice for *intracellular* target delivery and in general for sub-cellular studies, with some noticeable exceptions.(J. Liu, Cho, Cui, & Irudayaraj, 2014; Macias-Romero et al., 2014; Nakayama et al., 2007) The particles in fact tend to remain localized in specific compartments after internalization (endosomes) weakly interacting with the rest of the cell body.(Staedler et al., 2012; Staedler et al., 2015) Under this respect, they are better suited to label specific individual cells in a sample.

2) Differently from most quantum dots, HNPs do not contain heavy elements (*e.g.,* Cd, Hg), known to be highly cytotoxic. However, their effects on cells viability, proliferation, metabolism, etc. should be assessed for each sample type as the interaction depends not only on the particle chemical composition but is also affected by its structural stability at different pHs (to avoid release of ions), its shape and size, surface charge, and concentration. Most importantly, HNPs-cells interaction is critically sensitive to the cell type under study. Note that for most bio-imaging applications, particles should be coated (e.g., with a polymer) and specific functionalization agents could be attached to the coating to selectively target cell membrane receptors.(Débarre et al., 2005; Hsieh, Grange, Pu, & Psaltis, 2010; Nami, Y.,

Roxanne, E., & Periklis, 2018; Passemard et al., 2015) These additional procedures, common to other nanotechnology approaches, can further modify the toxicity profile of the particle. So far, most of the studies on HNPs-cell interaction (including high throughput multi-parameter analysis) have been performed on $BaTiO_3$, BFO, and ZnO nanoparticles. The former two seem to affect weakly the cells and notably they have been proven compatible with stem-cell differentiation.(Dubreil et al., 2017; Li et al., 2016; Nami et al., 2018)

3) HNP optical excitation and emission properties are the ones, which stand out making the difference with other approaches and could motivate their selection for specific imaging tasks. Firstly, the fact that the detected signals rely on non-parametric optical generation (SHG and THG) implies that signal stability over time is not affected by blinking or bleaching.(Le Xuan et al., 2008; Staedler et al., 2012) In fact, the light-particle interaction does not require sequential excitation and emission processes involving excited electronic states, which always possess a non-vanishing probability to lead the system into a dark state (e.g., surface trapping in quantum dots). Similarly, for HNPs minimal excess energy is deposed on the particle (contrary to the case of fluorescent probes), which helps preventing sample photo-degradation by cumulative heat deposition. A crucial role for motivating the selection of HNPs against other nanoprobes is played by the possibility to tune the excitation wavelength in a large spectral region spanning from near UV to mid-IR, according to the transparency region of each specific HNP material. The advantages opened by this possibility are multi-fold: the laser wavelength can be selected i) to avoid autofluorescence excitation and overlap with the fluorescent staining agents present in the sample; ii) to best match the sample optical properties to increase imaging penetration depth.(Grange, Lanvin, Hsieh, Pu, & Psaltis, 2011; Pantazis, Maloney, Wu, & Fraser, 2010; Rogov et al., 2015) In thick samples, the imaging depth critically depends on light scattering and absorption along the excitation

path. As scattering is monotonously decreasing with wavelength, longer wavelengths are more favourable provided that the maxima of water absorption are avoided. With the advent of new light sources in the near infrared (NIR), new spectral regions amenable for imaging have been added to the traditional transparency tissue window (NIR I, 600-1000 nm), namely NIR II (1100-1350 nm) and NIR-III (1600-1870 nm).(Sordillo, Pu, Pratavieira, Budansky, & Alfano, 2014) Very interestingly, HNPs can be excited within these NIR regions, and the harmonic signals produced conveniently lie in the visible, where water absorption is minimal. Note that the scattering properties of the sample do not constitute a limiting factor for the detection of the signal generated; on the contrary scattering can be convenient for increasing the fraction of signal photons detected in the backward direction, which is the standard collection geometry for *in vivo* studies.(Débarre, Olivier, & Beaurepaire, 2007)

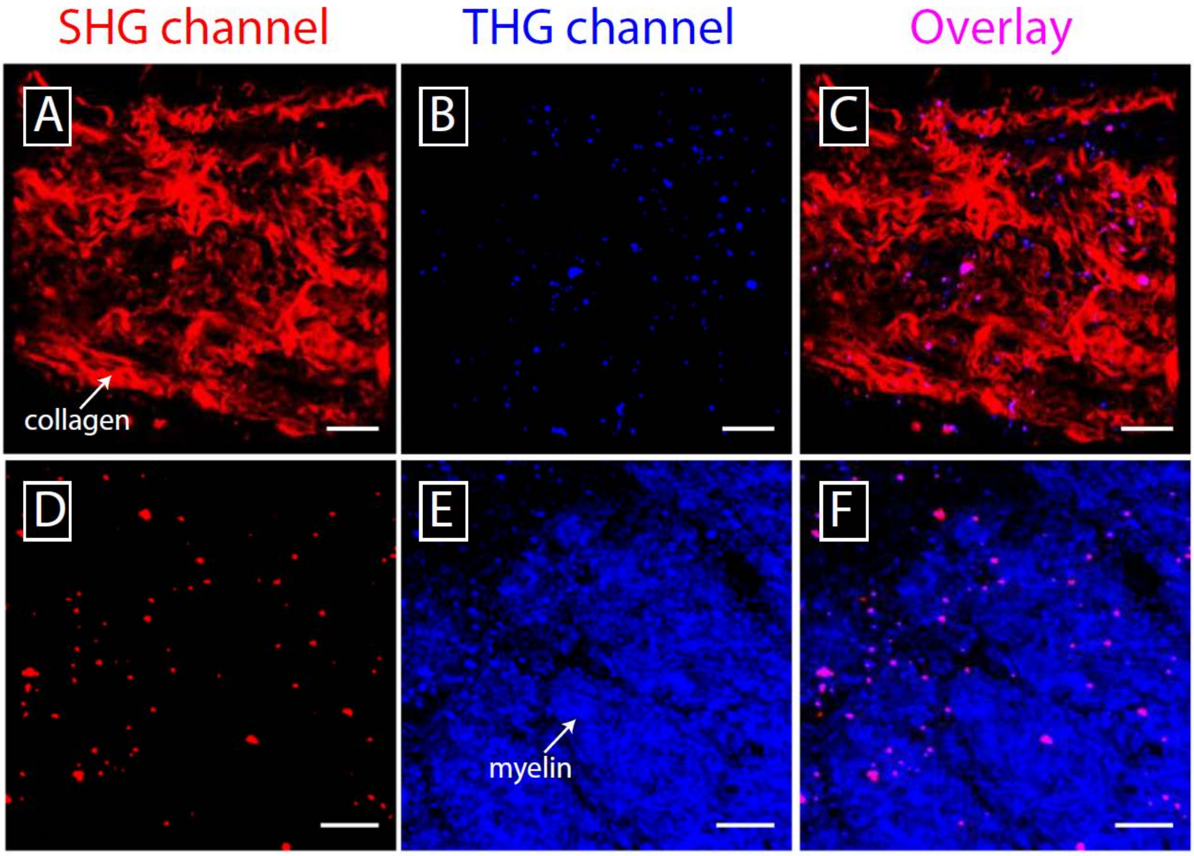

Figure 4. *First row:* HNPs on a collagen-rich tissue region. In the SHG channel, HNPs are not distinguishable from the background, while they appear with no hindrance in the THG channel. *Second row:* HNPs in a myelin-rich region. Here HNPs are visible with high contrast exclusively the SHG channel. Laser excitation 1300 nm. Scale bar 20 µm. (Adapted with permission from Dubreil et al., 2017. Copyright 2017 American Chemical Society.)

The selectivity in the retrieval of HNPs in optically congested environments (*e.g.*, tissue, body fluids) beside the aforementioned minimization of (auto-)fluorescence hindrance by wavelength selection, can be further improved using a multi-order harmonic approach.(Dubreil et al., 2017; Rogov et al., 2015) When excited in the NIR-II region, for example at 1300 nm, HNPs emit simultaneously at 650 nm (SHG) and 433 nm (THG). These two signals can be conveniently collected in parallel and correlated to identify nanoparticles against any fluorescence background but also against endogenous sources of harmonic emission in tissues such as collagen (SHG)(Williams, Zipfel, & Webb, 2005) and lipids (THG).(Débarre et al., 2005) In fact, while these endogenous structures are known to emit efficiently only at one nonlinear order (either SHG either THG), HNPs generate both harmonic signals. As reported in Fig. 4, this characteristic deems essential for identifying them in different tissue compartments. In panel A, an extended collagen network is visible by SHG. The eventual presence of structures or cells labelled by HNPs is not apparent in this channel, however if observed in the THG channel only HNPs appear thanks to their strong emission. Similarly, the lipid composition of myelin, a fatty substance surrounding nerve axons, appear in the THG channel hindering the presence of HNPs (panel E). In this case, the SHG channel provides background-free detection of the particles. Note that the excitation and collection of SHG and THG channel are implemented simultaneously under standard conditions for multiphoton imaging. However, a THG signal can be detected only when using laser excitation above 1100 nm, because of the transmission cut-off of microscope regular optics < 350 nm.

Bibliography

Alexiewicz, W., Ozgo, Z., & Kielich, S. (1975). Spectral theory of third-harmonic light scattering by molecular liquids. *Acta Phys. Pol. A, 48*, 243-252.

Ali, R. F., & Gates, B. D. (2018). Synthesis of Lithium Niobate Nanocrystals with Size Focusing through an Ostwald Ripening Process. *Chemistry of Materials, 30*(6), 2028-2035.

Baranov, D. G., Zuev, D. A., Lepeshov, S. I., Kotov, O. V., Krasnok, A. E., Evlyukhin, A. B., & Chichkov, B. N. (2017). All-dielectric nanophotonics: the quest for better materials and fabrication techniques. *Optica, 4*(7), 814-825. doi:10.1364/OPTICA.4.000814

Bonacina, L., Mugnier, Y., Courvoisier, F., Le Dantec, R., Extermann, J., Lambert, Y., . . . Wolf, J. P. (2007). Polar Fe(IO3)(3) nanocrystals as local probes for nonlinear microscopy. *Applied Physics B-Lasers and Optics, 87*(3), 399-403. doi:DOI 10.1007/s00340-007-2612-z

Bosshard, C., Gubler, U., Kaatz, P., Mazerant, W., & Meier, U. (2000). Non-phase-matched optical third-harmonic generation in noncentrosymmetric media: cascaded second-order contributions for the calibration of third-order nonlinearities. *Physical Review B, 61*(16), 10688.

Boyd, R. W. (2003). *Nonlinear optics*: Academic press.

Caruntu, D., Rostamzadeh, T., Costanzo, T., Parizi, S. S., & Caruntu, G. (2015). Solvothermal synthesis and controlled self-assembly of monodisperse titanium-based perovskite colloidal nanocrystals. *Nanoscale, 7*(30), 12955-12969.

Clarke, G., Rogov, A., McCarthy, S., Bonacina, L., Gun'ko, Y., Galez, C., . . . Prina-Mello, A. (2018). Preparation from a revisited wet chemical route of phase-pure, monocrystalline and SHG-efficient BiFeO 3 nanoparticles for harmonic bio-imaging. *Scientific Reports, 8*(1), 10473.

Clays, K., & Persoons, A. (1991). Hyper-Rayleigh scattering in solution. *Physical Review Letters, 66*(23), 2980.

Cyvin, S., Rauch, J., & Decius, J. (1965). Theory of Hyper-Raman Effects (Nonlinear Inelastic Light Scattering): Selection Rules and Depolarization Ratios for the Second-Order Polarizability. *The Journal of Chemical Physics, 43*(11), 4083-4095.

Danks, A., Hall, S., & Schnepp, Z. (2016). The evolution of 'sol–gel'chemistry as a technique for materials synthesis. *Materials Horizons, 3*(2), 91-112.

Débarre, D., Olivier, N., & Beaurepaire, E. (2007). Signal epidetection in third-harmonic generation microscopy of turbid media. *Optics express, 15*(14), 8913-8924.

Débarre, D., Supatto, W., Pena, A.-M., Fabre, A., Tordjmann, T., Combettes, L., . . . Beaurepaire, E. (2005). Imaging lipid bodies in cells and tissues using third-harmonic generation microscopy. *Nature methods, 3*(1), 47-53.

Deniset-Besseau, A., Duboisset, J., Benichou, E., Hache, F., Brevet, P.-F., & Schanne-Klein, M.-C. (2009). Measurement of the second-order hyperpolarizability of the collagen triple helix and determination of its physical origin. *The Journal of Physical Chemistry B, 113*(40), 13437-13445.

Dubreil, L., Leroux, I., Ledevin, M., Schleder, C., Lagalice, L., Lovo, C., . . . Rouger, K. (2017). Multi-Harmonic Imaging in the Second Near-Infrared Window of Nanoparticle-Labeled Stem Cells as Monitoring Tool in Tissue Depth. *ACS Nano, 11*(7), 6672-6681.

Ghosh, S., Dasgupta, S., Sen, A., & Sekhar Maiti, H. (2005). Low-temperature synthesis of nanosized bismuth ferrite by soft chemical route. *Journal of the American Ceramic Society, 88*(5), 1349-1352.

Grange, R., Lanvin, T., Hsieh, C. L., Pu, Y., & Psaltis, D. (2011). Imaging with second-harmonic radiation probes in living tissue. *Biomedical Optics Express, 2*(9), 2532-2539.

Gubler, U., & Bosshard, C. (2002). Molecular Design for Third-Order Nonlinear Optics. In *Polymers for Photonics Applications I. Advances in Polymer Science*. Berlin, heidelberg: Springer.

Hendrickx, E., Clays, K., & Persoons, A. (1998). Hyper-Rayleigh scattering in isotropic solution. *Accounts of Chemical Research, 31*(10), 675-683.

Hsieh, C. L., Grange, R., Pu, Y., & Psaltis, D. (2010). Bioconjugation of barium titanate nanocrystals with immunoglobulin G antibody for second harmonic radiation imaging probes. *Biomaterials, 31*(8), 2272-2277. doi:DOI 10.1016/j.biomaterials.2009.11.096

Jacobsohn, M., & Banin, U. (2000). Size dependence of second harmonic generation in CdSe nanocrystal quantum dots. *The Journal of Physical Chemistry B, 104*(1), 1-5.

Joulaud, C., Mugnier, Y., Djanta, G., Dubled, M., Marty, J. C., Galez, C., . . . Le Dantec, R. (2013). Characterization of the nonlinear optical properties of nanocrystals by Hyper Rayleigh Scattering. *Journal of Nanobiotechnology, 11*, S8. doi:Artn S8

Doi 10.1186/1477-3155-11-S1-S8

Kim, E., Steinbr\"uck, A., Buscaglia, M. T., Buscaglia, V., Pertsch, T., & Grange, R. (2013). Second-Harmonic Generation of Single BaTiO3 Nanoparticles down to 22 nm Diameter. *ACS Nano, 7*(6), 5343-5349.

Knabe, B., Buse, K., Assenmacher, W., & Mader, W. (2012). Spontaneous polarization in ultrasmall lithium niobate nanocrystals revealed by second harmonic generation. *Physical Review B, 86*(19), 195428.

Kuznetsov, A. I., Miroshnichenko, A. E., Brongersma, M. L., Kivshar, Y. S., & Luk'yanchuk, B. (2016). Optically resonant dielectric nanostructures. *Science, 354*(6314), aag2472.

Ladj, R., Bitar, A., Eissa, M., Mugnier, Y., Le Dantec, R., Fessi, H., & Elaissari, A. (2013). Individual inorganic nanoparticles: preparation, functionalization and in vitro biomedical diagnostic applications. *Journal of Materials Chemistry B, 1*(10), 1381-1396.

Ladj, R., El Kass, M., Mugnier, Y., Le Dantec, R., Fessi, H., Galez, C., & Elaissari, A. (2012). SHG Active Fe(IO3)3 Particles: From Spherical Nanocrystals to Urchin-Like Microstructures through the Additive-Mediated Microemulsion Route. *Cryst. Growth Des., dx.doi.org/10.1021/cg3009915*.

Le Dantec, R., Mugnier, Y., Djanta, G., Bonacina, L., Extermann, J., Badie, L., . . . Galez, C. (2011). Ensemble and Individual Characterization of the Nonlinear Optical Properties of ZnO and BaTiO3 Nanocrystals. *Journal of Physical Chemistry C, 115*(31), 15140-15146. doi:Doi 10.1021/Jp200579x

Le Floc'h, V., Brasselet, S., Roch, J.-F., & Zyss, J. (2003). Monitoring of orientation in molecular ensembles by polarization sensitive nonlinear microscopy. *The Journal of Physical Chemistry B, 107*(45), 12403-12410.

Le Xuan, L., Zhou, C., Slablab, A., Chauvat, D., Tard, C., Perruchas, S., . . . Roch, J. F. (2008). Photostable second-harmonic generation from a single KTiOPO4 nanocrystal for nonlinear microscopy. *Small, 4*(9), 1332-1336. doi:DOI 10.1002/smll.200701093

Li, J. H., Qiu, J. C., Guo, W. B., Wang, S., Ma, B. J., Mou, X. N., . . . Liu, H. (2016). Cellular internalization of LiNbO3 nanocrystals for second harmonic imaging and the effects on stem cell differentiation. *Nanoscale, 8*(14), 7416-7422. doi:10.1039/c6nr00785f

Liu, J., Cho, I.-H., Cui, Y., & Irudayaraj, J. (2014). Second Harmonic Super-Resolution Microscopy for Quantification of mRNA at Single Copy Sensitivity. *ACS Nano, 8*(12), 12418-12427.

Liu, S., Huang, L., Li, W., Liu, X., Jing, S., Li, J., & O'Brien, S. (2015). Green and scalable production of colloidal perovskite nanocrystals and transparent sols by a controlled self-collection process. *Nanoscale, 7*(27), 11766-11776.

Livage, J., & Sanchez, C. (1992). Sol-gel chemistry. *Journal of Non-Crystalline Solids, 145*, 11-19.

Lombardi, J., Pearsall, F., Li, W., & O'Brien, S. (2016). Synthesis and dielectric properties of nanocrystalline oxide perovskites,[KNbO 3] 1− x [BaNi 0.5 Nb 0.5 O 3− δ] x, derived from potassium niobate KNbO 3 by gel collection. *Journal of Materials Chemistry C, 4*(34), 7989-7998.

Macias-Romero, C., Didier, M. E. P., Zubkovs, V., Delannoy, L., Dutto, F., Radenovic, A., & Roke, S. (2014). Probing rotational and translational diffusion of nanodoublers in living cells on microsecond time scales. *Nano Letters*.

Malgrange, C., Ricolleau, C., & Lefaucheux, F. (2012). *Symétrie et propriétés physiques des cristaux*: EDP sciences.

Modeshia, D. R., & Walton, R. I. (2010). Solvothermal synthesis of perovskites and pyrochlores: crystallisation of functional oxides under mild conditions. *Chemical Society Reviews, 39*(11), 4303-4325.

Mohanty, D., Chaubey, G. S., Yourdkhani, A., Adireddy, S., Caruntu, G., & Wiley, J. B. (2012). Synthesis and piezoelectric response of cubic and spherical LiNbO3 nanocrystals. *Rsc Advances, 2*(5), 1913-1916. doi:Doi 10.1039/C2ra00628f

Morita, R., & Yamashita, M. (1993). Relationship between 2nd-Order and 3rd-Order Nonlinear-Optical Susceptibilities Due to Electronic Polarization. *Japanese Journal of Applied Physics Part 2-Letters, 32*(7A), L905-L907. doi:Doi 10.1143/Jjap.32.L905

Mugnier, Y., Houf, L., El-Kass, M., Le Dantec, R., Hadji, R., Vincent, B., . . . Galez, C. (2011). In Situ Crystallization and Growth Dynamics of Acentric Iron Iodate Nanocrystals in w/o Microemulsions Probed by Hyper-Rayleigh Scattering Measurements. *Journal of Physical Chemistry C, 115*(1), 23-30. doi:Doi 10.1021/Jp105638s

Multian, V. V., Riporto, J., Urbain, M., Mugnier, Y., Djanta, G., Beauquis, S., . . . Le Dantec, R. (2018). Averaged Third-Order Susceptibility of ZnO Nanocrystals from Third Harmonic Generation and Third Harmonic Scattering. *Optical Materials, accepted*. doi:https://doi.org/10.1016/j.optmat.2018.07.032

Nakayama, Y., Pauzauskie, P. J., Radenovic, A., Onorato, R. M., Saykally, R. J., Liphardt, J., & Yang, P. D. (2007). Tunable nanowire nonlinear optical probe. *Nature, 447*(7148), 1098-U1098. doi:Doi 10.1038/Nature05921

Nami, S., Y., S. A., Roxanne, T., E., C. B., & Periklis, P. (2018). Effective Labeling of Primary Somatic Stem Cells with BaTiO3 Nanocrystals for Second Harmonic Generation Imaging. *Small, 14*(8), 1703386. doi:doi:10.1002/smll.201703386

Nappa, J., Revillod, G., Russier-Antoine, I., Benichou, E., Jonin, C., & Brevet, P. (2005). Electric dipole origin of the second harmonic generation of small metallic particles. *Physical Review B, 71*(16), 165407.

Niederberger, M., & Garnweitner, G. (2006). Organic reaction pathways in the nonaqueous synthesis of metal oxide nanoparticles. *Chemistry–A European Journal, 12*(28), 7282-7302.

Nye, J. F. (1985). *Physical properties of crystals: their representation by tensors and matrices*: Oxford university press.

Nyman, M., Anderson, T. M., & Provencio, P. P. (2009). Comparison of aqueous and non-aqueous soft-chemical syntheses of lithium niobate and lithium tantalate powders. *Crystal Growth and Design, 9*(2), 1036-1040.

Ono, S., & Hirano, S. i. (1997). Patterning of lithium niobate thin films derived from aqueous solution. *Journal of the American Ceramic Society, 80*(10), 2533-2540.

Pantazis, P., Maloney, J., Wu, D., & Fraser, S. E. (2010). Second harmonic generating (SHG) nanoprobes for in vivo imaging. *Proceedings of the National Academy of Sciences of the United States of America, 107*(33), 14535-14540. doi:DOI 10.1073/pnas.1004748107

Passemard, S. e., Staedler, D., Sonego, G., Magouroux, T., Schneiter, G. S. e., Juillerat-Jeanneret, L., . . . Gerber-Lemaire, S. (2015). Functionalized bismuth ferrite harmonic nanoparticles for cancer cells labeling and imaging. *Journal of Nanoparticle Research, 17*(10), 1-13.

Polking, M. J., Alivisatos, A. P., & Ramesh, R. (2015). Synthesis, physics, and applications of ferroelectric nanomaterials. *MRS Communications, 5*(1), 27-44.

Riporto, J., Demierre, A., Kilin, V., Balciunas, T., Schmidt, C., Campargue, G., . . . Wolf, J.-P. (2018). Bismuth ferrite dielectric nanoparticles excited at telecom wavelengths as multicolor sources by second, third, and fourth harmonic generation. *Nanoscale, 10*(17), 8146-8152.

Rodriguez, E. V., de Araújo, C. B., Brito-Silva, A. M., Ivanenko, V., & Lipovskii, A. (2009). Hyper-Rayleigh scattering from BaTiO3 and PbTiO3 nanocrystals. *Chemical Physics Letters, 467*(4-6), 335-338.

Rogov, A., Irondelle, M., Ramos Gomes, F., Bode, J., Staedler, D., Passemard, S., . . . Wolf, J.-P. (2015). Simultaneous Multiharmonic Imaging of Nanoparticles in Tissues for Increased Selectivity. *ACS Photonics, 2*(10), 1416-1422. doi:10.1021/acsphotonics.5b00289

Roke, S., & Gonella, G. (2012). Nonlinear light scattering and spectroscopy of particles and droplets in liquids. *Annual review of physical chemistry, 63*, 353-378.

Russier-Antoine, I., Benichou, E., Bachelier, G., Jonin, C., & Brevet, P. (2007). Multipolar contributions of the second harmonic generation from silver and gold nanoparticles. *The Journal of Physical Chemistry C, 111*(26), 9044-9048.

Sandeau, N., Le Xuan, L., Chauvat, D., Zhou, C., Roch, J. F., & Brasselet, S. (2007). Defocused imaging of second harmonic generation from a single nanocrystal. *Optics express, 15*(24), 16051-16060.

Schmidt, C., Riporto, J., Uldry, A., Rogov, A., Mugnier, Y., Le Dantec, R., . . . Bonacina, L. (2016). Multi-Order Investigation of the Nonlinear Susceptibility Tensors of Individual Nanoparticles. *Scientific Reports, 6*, 25415.

Schwung, S., Rogov, A., Clarke, G., Joulaud, C., Magouroux, T., Staedler, D., . . . Galez, C. (2014). Nonlinear optical and magnetic properties of BiFeO3 harmonic nanoparticles. *Journal of Applied Physics, 116*(11), 114306.

Selbach, S. M., Einarsrud, M. A., Tybell, T., & Grande, T. (2007). Synthesis of BiFeO3 by wet chemical methods. *Journal of the American Ceramic Society, 90*(11), 3430-3434.

Smith, B. R., & Gambhir, S. S. (2017). Nanomaterials for in vivo imaging. *Chemical reviews, 117*(3), 901-986.

Sordillo, L. A., Pu, Y., Pratavieira, S., Budansky, Y., & Alfano, R. R. (2014). Deep optical imaging of tissue using the second and third near-infrared spectral windows. *Journal of biomedical optics, 19*(5), 056004-056004.

Staedler, D., Magouroux, T., Hadji, R., Joulaud, C., Extermann, J., Schwungi, S., . . . Wolf, J. P. (2012). Harmonic Nanocrystals for Biolabeling: A Survey of Optical Properties and Biocompatibility. *ACS Nano, 6*(3), 2542-2549. doi:Doi 10.1021/Nn204990n

Staedler, D., Passemard, S., Magouroux, T., Rogov, A., Maguire, C. M., Mohamed, B. M., . . . Wolf, J.-P. (2015). Cellular Uptake and Biocompatibility of Bismuth Ferrite Harmonic Advanced Nanoparticles. *Nanomedicine: NBM, 11(4)*, 815-828.

Terhune, R., Maker, P., & Savage, C. (1965). Measurements of nonlinear light scattering. *Physical Review Letters, 14*(17), 681.

Tytus, T., Phelan, O., Urbain, M., Clarke, G., Riporto, J., Le Dantec, R., . . . Mugnier, Y. (2018). Preparation and preliminary non-linear optical properties of BiFeO3 nanocrystal suspensions from a simple, chelating agent-free precipitation route. *Journal of Nanomaterials*.

Van Steerteghem, N., Clays, K., Verbiest, T., & Van Cleuvenbergen, S. (2017). Third-Harmonic Scattering for Fast and Sensitive Screening of the Second Hyperpolarizability in Solution. *Analytical chemistry, 89*(5), 2964-2971.

Williams, R. M., Zipfel, W. R., & Webb, W. W. (2005). Interpreting second-harmonic generation images of collagen I fibrils. *Biophysical Journal, 88*(2), 1377-1386. doi:DOI 10.1529/biophysj.104.047308

Yang, X.-l., & Xie, S.-w. (1995). Expression of third-order effective nonlinear susceptibility for third-harmonic generation in crystals. *Applied optics, 34*(27), 6130-6135.

Yerlikaya, C., Ullah, N., Kamali, A. R., & Kumar, R. V. (2016). Size-controllable synthesis of lithium niobate nanocrystals using modified Pechini polymeric precursor method. *Journal of Thermal Analysis and Calorimetry, 125*(1), 17-22.